A new perspective of permafrost boundaries in France during the Last Glacial Maximum

Kim H. Albers[1], Patrick Ludwig[1], Pascal Bertran[2,3], Pierre Antoine[4], Xiaoxu Shi[5], Gerrit Lohmann[5,6], and Joaquim G. Pinto[1]

[1]Institute of Meteorology and Climate Research, Karlsruhe Institute of Technology, Karlsruhe, Germany
[2]Inrap, Bègles, France
[3]PACEA, CNRS-Université de Bordeaux, Pessac, France
[4]Laboratoire de Géographie Physique, CNRS, Meudon Cedex, France
[5]Alfred Wegener Institute, Helmholtz Centre for Polar and Marine Research, Bremerhaven, Germany
[6]MARUM and Institute of Environmental Physics, University of Bremen, Bremen, Germany

Correspondence: Kim H. Albers (kim.albers@kit.edu)

Abstract. During the Last Glacial Maximum (LGM), a very cold and dry period around 26.5 to 19 thousand years ago, permafrost was widespread across Europe. In this work, we evaluate the potential of regional climate model simulations to reconstruct the permafrost distribution in western Europe during the LGM. With this aim, criteria for possible thermal contraction cracking of the ground are applied to climate model data for the first time. These criteria serve as a precondition for the development of ice and sand wedges, which are a common proxy for past permafrost. Our results show that the permafrost and ground cracking distribution in Europe during the LGM are not consistent with a large-scale circulation with prevailing westerly winds. However, a colder and with regard to proxy data more realistic version of the LGM climate is achieved given more frequent easterly winds conditions. Whereas the permafrost extent and ground cracking regions in the global climate model simulation deviate from proxy evidence, they are in good agreement in the regional counterpart. Given the appropriate forcing, an added value of the regional climate model simulation can thus be achieved. Furthermore, the model data provide evidence that thermal contraction cracking occurred in Europe during the LGM also south of the probable permafrost border. This enables the reconsideration of the significance of ice wedge pseudomorphs and sand wedge casts to understand past climate variations.

1 Introduction

Permafrost is an important component of the climate system and is particularly sensitive to variations of climate. Permafrost is defined as ground - including soil, rock, ice and organic material - that remains at or below 0 °C for at least two consecutive years (van Everdingen, 2005). In recent decades, thawing of permafrost soils has affected many high-latitude regions, and thawing is most likely to accelerate in the near and long-term future (IPCC, 2013, 2019; Harris et al., 2009). While enhanced greenhouse gas forcing leads to warming temperatures and thus to permafrost thawing, the thawing itself leads to the release of greenhouse gases that were previously bound within the frozen soils. Thereby, the greenhouse effect is enhanced which leads to further warming of the climate, in a positive feedback (e.g., IPCC, 2019; Liu and Jiang, 2016a; Schuur et al., 2015).

Current climate model simulations project a large range of uncertainties regarding the decrease of permafrost areas (e.g., IPCC, 2019; Schuur et al., 2015). The models are calibrated for present-day conditions, under which they are well tested. However, the responses of the models to the same forcing vary by several orders of magnitude (e.g., Braconnot et al., 2012; Cleator et al.,

25 2020; IPCC, 2013, 2019). It is therefore necessary to evaluate the climate models under a wider range of climate conditions. This can be achieved by simulating past climates and comparing the results with proxy evidence from Quaternary sequences (Braconnot et al., 2012; Harrison et al., 2015; Smerdon, 2012).

During the Last Glacial Maximum (LGM; Clark et al., 2009; Mix et al., 2001) corresponding to around 26.5 to 19 thousand years (ka) before present, huge ice sheets covered large parts of the Northern Hemisphere, modifying the surface albedo and

30 orography (Hughes et al., 2015; Ullman et al., 2014), and enhanced sea ice cover modified heat fluxes between the ocean and atmosphere (Flückiger et al., 2008). The sea level was about $130\,\mathrm{m}$ lower than today (Lambeck et al., 2014) and the greenhouse gas concentrations were at a historical minimum with values less than half of its current concentrations (Clark et al., 2009; Monnin et al., 2001). Lower greenhouse gas concentrations favoured the growth of C4 over C3 plants (Prentice and Harrison, 2009), although only C3 plants have actually been identified in European loess (Hatté et al., 1998, 2001).

35 Globally, this hampered the development of trees (Woillez et al., 2011), resulting in less productive terrestrial ecosystems and more open vegetation (Bartlein et al., 2011). Ultimately, this resulted in easily erodible soils, whose contribution to the dust cycle increased (Prospero et al., 2002; Ray and Adams, 2001). These boundary conditions and forcing led to a substantially different climate than today. In general, the LGM was colder, drier and windier period in Earths' history compared to the recent climate (e.g., Annan and Hargreaves, 2013; Bartlein et al., 2011; Löfverström et al., 2014). The global and annual mean

40 surface air temperatures were about $4\,^{\circ}\mathrm{C}$ colder than today, with differences reaching up to $14\,^{\circ}\mathrm{C}$ close to the LGM ice sheets e.g., in Central Europe (e.g., Annan and Hargreaves, 2013; Bartlein et al., 2011; Clark et al., 2009; Pfahl et al., 2015; Ludwig et al., 2017). The atmospheric circulation in the North Atlantic region varied considerably from the current conditions mainly due to the direct influence of the altered topography by ice sheets (Justino and Peltier, 2005; Merz et al., 2015). A planetary large-scale atmospheric wave with an amplitude much larger than today was induced, with a deep trough downstream of the

45 Laurentide ice sheet. This led to a generally more zonal orientation of the North Atlantic jet stream (Löfverström et al., 2014). Additionally, the jet was enhanced and its position was shifted southward (e.g., Li and Battisti, 2008; Merz et al., 2015; Pausata et al., 2011). The storm track during the LGM evolved accordingly (e.g., Löfverström et al., 2014; Ludwig et al., 2016; Raible et al., 2020), and extreme cyclones were more intense and characterized by less precipitation (Pinto and Ludwig, 2020). Thus, cyclones were able to trigger more frequent dust storms during the LGM (Antoine et al., 2009; Pinto and Ludwig, 2020; Sima

50 et al., 2009). Besides these dust storms, easterly winds induced by an anticyclone over the Fennoscandian ice sheet (FIS) were another important factor for the deposition of loess in Central and Western Europe (Krauß et al., 2016; Schaffernicht et al., 2020; Stevens et al., 2020).

At the same time, adjacent areas south of the FIS were widely affected by permafrost (Kitover et al., 2013; Levavasseur et al., 2011; Saito et al., 2013; Vandenberghe et al., 2014; Washburn, 1979). The past permafrost distribution is usually inferred from

55 the occurrence of a variety of fossil periglacial features, among which ice wedge pseudomorphs are the most reliable and widespread (e.g., Bertran et al., 2014; Péwé, 1966; Vandenberghe et al., 2014). Ice wedges develop within perennially frozen

ground, when temperature drops quickly and the ground experiences thermal contraction cracking. Open cracks may be filled with water in spring supplied from melting snow, which freezes at depth and forms ice veins. When this ground cracking process is repeated over many (but not necessarily consecutive) years, the cracks grow and widen, leading to the typical shape

60 of ice wedges (Murton, 2013). When the ice is replaced by other sediments due to melting, the features are called ice wedge pseudomorphs. Today, ice wedges are mostly active in continuous permafrost environments (Fortier and Allard, 2005; Kokelj et al., 2014; Matsuoka et al., 2018; Péwé, 1966). Open cracks may also be filled with wind-blown sand, which gives rise to sand wedges, or by both ice and sand (composite wedges). Active sand wedges are found today primarily in areas characterised by continuous permafrost and limited snow and vegetation cover, and with local sources of aeolian sediments such as in Antarctica

65 (Bockheim et al., 2009; Levy et al., 2008; Pewe, 1959). However, Wolfe et al. (2018) showed that sand wedges can also develop in Canada in areas with deep seasonal ground freezing (i.e. without perennially frozen ground) in mineral soils close to dune fields. Thermal contraction cracking of the ground, which is usually the limiting factor for wedge growth in current densely vegetated areas (e.g. shrub tundra and taiga; Kokelj et al., 2014; Mackay and Burn, 2002), can actually occur at low frequency in mid-latitude, cool temperate regions in grounds devoid of tall vegetation and snow (Barosh, 2000; Okkonen et al., 2020;

70 Washburn, 1963).

Many attempts at reconstructing the past permafrost distribution in Europe using field proxies have been performed during the last decades. Based on the assumption that both active ice wedges and sand wedges are associated with continuous permafrost and possibly with widespread discontinuous permafrost (Burn, 1990; Romanovskij, 1973), some of the earliest reconstitutions (e.g., Vandenberghe et al., 2014) proposed that Europe was affected by permafrost as far south as the 43.5° N latitude. However,

75 a detailed analysis of periglacial features in France by Andrieux et al. (2016b, 2018) demonstrated that typical ice wedge pseudomorphs are exclusively found north of latitude 47.5° N, whereas sand wedge casts occur at lower latitude at the periphery of aeolian sandsheets. A correlation between wedge depth and latitude has also been highlighted, which strongly suggests that the southernmost shallow sand wedges developed in regions where perennial ice could not form, i.e. without permafrost or with sporadic permafrost.

80 Multiple attempts have also been performed to infer the LGM permafrost occurrence from climate model data. Liu and Jiang (2016b) considering both direct and indirect methods. The simplest indirect method is based on the modelled mean annual air temperature (MAAT). Threshold values for permafrost occurrence were adapted according to ground texture (Vandenberghe et al., 2012). However, this method only provides a rough estimate of permafrost extension, since a variety of other factors are known to impact ground temperatures, including water content, vegetation and snow cover. Particularly, the insulating effects

85 of snow and vegetation cover may be responsible for an offset of up to $6\,°C$ between MAAT and the mean annual ground surface temperature (MAGST). On the other hand, variations in ground thermal conductivity (depending on texture and water content) may result in an offset of $2\,°C$ between MAGST and the temperature at the top of permafrost (TTOP) (e.g., Smith and Riseborough, 2002; Throop et al., 2012). A refined indirect method is the use of the surface frost index (SFI, Nelson and Outcalt, 1987), which corresponds to the ratio between frost and thaw penetration depths and takes the effects of snow

90 in account. The SFI has been used in several studies, with only minor changes of the original method. For example, monthly model output was used instead of summing up daily air temperatures (e.g., Frauenfeld et al., 2007; Liu and Jiang, 2016b).

Slater and Lawrence (2013) weighted the snow depth for each month to consider snow accumulation effects, while Stendel and Christensen (2002) replaced the surface air temperature with the temperature of the deepest ground layer (5.7 m deep) to investigate permafrost degradation due to current global warming. For the direct method, the modelled ground temperatures

95 below $0\,°C$ are used to diagnose permafrost. The studies differ slightly in the depth of the considered ground temperatures (e.g., Liu and Jiang, 2016a, b; Saito et al., 2013; Slater and Lawrence, 2013).

Studies investigating the permafrost limits during the LGM using global climate simulations have failed so far to reproduce appropriately the permafrost extent as reconstructed from field proxies (e.g., Andrieux et al., 2016b; Levavasseur et al., 2011; Ludwig et al., 2017). However, there is evidence for improvements when using the data from regional climate simulations (e.g.,

100 Ludwig et al., 2017, 2019). The aim of this study is (1) to explore the possible benefit of using regional climate model data to improve the permafrost representation over France, (2) to decipher how the atmospheric circulation affect the permafrost boundaries in the models and finally, (3) to test the role of ground thermal contraction cracking in wedge development during the LGM.

In section 2 we introduce the adaptions made to the regional climate model to be compliant with LGM boundary conditions and

105 describe the global simulations that provide the initial and boundary conditions. Further, we give an overview of the different methods used to derive the LGM permafrost distribution in France. In section 3 we describe the general characteristics and differences of the LGM climate based on the global and regional climate model data and present the permafrost and ground cracking distribution based on regional climate model data. Finally, we discuss and summarize the results in section 4.

2 Data and Methods

110 In this study, LGM simulations of two global climate models, namely MPI-ESM-P (MPI; Jungclaus et al., 2013; Stevens et al., 2013) and ECHAM6-FESOM (AWI; Sidorenko et al., 2015; Lohmann et al., 2020), are dynamically downscaled with the Weather Research and Forecast model (WRF; Skamarock et al., 2008). Both global models share the same atmospheric component ECHAM6 but different modules for the ocean. The MPIOM (Marsland et al., 2003) is coupled within the MPI-ESM-P, forming the well established global climate model that took part in several CMIPs. In AWI-ESM, the FESOM ocean

115 model(Wang et al., 2014) featuring an unstructured mesh as well as a multi-resolution approach is used with a relatively high resolution of less than $30\,km$ north of $50°$ N. The atmospheric grid applied in the MPI and AWI experiment is T63 (roughly 1.9 degree spatially) with 47 unevenly distributed vertical levels. The simulations follow either the PMIP3 (MPI; Braconnot et al., 2012; http://pmip3.lsce.ipsl.fr/) or PMIP4 protocol (AWI; Kageyama et al., 2017), where the boundary conditions (solar constant, orbital parameters, greenhouse gases) are set accordingly to best estimate the LGM boundary conditions. The AWI-

120 ESM has been used in the recent CMIP6/PMIP4 intercomparisons (Brierley et al., 2020; Keeble et al., 2021; Kageyama et al., 2021) and was applied for the LGM (Lohmann et al., 2020). The ice sheet provided for PMIP3/CMIP5 LGM experiments is a blended product obtained by averaging three different ice sheet reconstructions: ICE-6G v2.0 (Peltier et al., 2015), MOCA (Tarasov and Peltier, 2003) and ANU (Lambeck et al., 2002), whereas the LGM topography in AWI experiment is configured based on the ICE6G reconstruction (Peltier et al., 2015). For the recent climate, the pre-industrial period (PI), corresponding

125   roughly to 1850, is used as a reference. The simulations follow again the PMIP3 (MPI; Taylor et al., 2012) or PMIP4 protocol
       (AWI; Eyring et al., 2016).

       Outputs from these global LGM simulations are used to drive the regional WRF simulations. The atmospheric boundary
       conditions are updated every six hours, SST and sea ice cover are updated daily. Apart from the different forcing, the set up
       of the two regional simulations is identical. The coastlines, ice sheet extent, trace gas conditions and orbital parameters are
130   adapted to LGM values according to the PMIP3 protocol (Ludwig et al., 2017). Modifications to the Alpine ice sheet are
       implemented according to Seguinot et al. (2018). Land use and vegetation cover is taken from the CLIMAP data set (CLIMAP
       Project Members, 1984). An overview of the used parametrization schemes in the WRF simulations is given in Table 1. The
       first model domain covers large parts of Europe with a horizontal resolution of 50 km (see Fig. 1) and 35 vertical layers up to
       150 hPa. The integration time step is 240 seconds. The second, nested domain covers southern parts of the FIS, the Alps and
135   France, where the latter represents the target region to assess the LGM permafrost limits in this study. Here, the horizontal
       resolution is 12.5 km and the integration time step is 48 seconds. The soil is separated into four layers, with representative
       depths of 5, 25, 70, and 150 cm. A total of 32 years are simulated for each global forcing simulation. The first two years are
       used as a spin up phase and are excluded from further analysis. This way it is ensured, that the atmosphere and soil properties
       and processes are in equilibrium.

140   The permafrost distribution is derived using the three different methods described in Sec. 1. For MAAT, the 2 m air temperature
       is considered. Threshold values were derived from data compiled from studies in current Arctic regions, where continuous
       permafrost is inferred for MAATs $< -8 \pm 2\,°C$, whereas discontinuous permafrost requires MAATs $< -4 \pm 2\,°C$ (e.g., Smith
       and Riseborough, 2002; Vandenberghe et al., 2012). The surface frost index (SFI) is based on the annual freezing and thawing
       degree-days (DDF and DDT, respectively) being the sum of daily air temperatures below or above $0\,°C$, respectively:

145    $$\mathrm{SFI} = \sqrt{\mathrm{DDF}}/(\sqrt{\mathrm{DDF}} + \sqrt{\mathrm{DDT}}).$$

       An SFI between 0.5 and 0.6 indicates sporadic permafrost, between 0.6 and 0.67 discontinuous permafrost, and above 0.67
       continuous permafrost (e.g., Nelson and Outcalt, 1987; Stendel and Christensen, 2002). For this indirect method, we use ground
       temperatures of the third layer at 78 cm and 70 cm for the global and regional simulations, respectively. With the direct method,
       permafrost is inferred when ground temperatures are at or below $0\,°C$.

150   Beyond the permafrost indices, ground cracking is assumed to be possible when two conditions derived from fieldwork by
       Matsuoka et al. (2018) are fulfilled simultaneously: A daily mean soil temperature below -5 $°C$ at a depth of 1 m and a temper-
       ature gradient in the upper meter of the ground below -7 $°C\,m^{-1}$. Due to higher ice content and higher organic carbon content
       of the ground, these values do not necessarily correspond exactly to those of France during the Pleistocene. We use the third
       soil layer again, with depths of 78 cm in the global simulations and of 70 cm in the regional simulations.

155   To evaluate the model simulations, the distribution of ice wedge pseudomorphs and sand wedges after Andrieux et al. (2016b)
       and Isarin et al. (1998) are considered.

3 Results

3.1 Global Boundary Conditions

Both global models simulate colder annual mean SSTs under LGM than under PI conditions (c.f. Fig. 2 a and b). For the
MPI model, a limited area with enhanced SSTs is simulated over the North Atlantic. This does not match with proxy data
(MARGO Project Members, 2009) and is a known issue for this and other PMIP3 models (e.g., Wang et al., 2013; Ludwig
et al., 2016, 2017). The AWI simulation does not show this warm anomaly over the North Atlantic and the SSTs are generally
colder. In the Arctic Ocean, the SSTs in the AWI simulation are considerably higher than in the MPI simulation. This can be
explained by the sea ice cover, which is lower in the AWI LGM simulation.

The analysis of wind speed at 300 hPa gives insights into the jet stream structure and strength, which are dominant factors of
the atmospheric large-scale circulation over the North Atlantic / European region. In agreement with Li and Battisti (2008),
both models show a stronger jet under LGM conditions compared to the simulations under PI conditions (c.f. Fig. 2 c and d).
This is particularly the case over the North Atlantic, south-eastward of the Laurentide ice sheet, where the wind speed is up
to 14 m/s higher in annual mean for LGM. On the other hand, the wind speed on both the southern and northern flanks of
the jet stream is actually 2-4 m/s weaker during the LGM, indicating a more constrained large-scale flow. Even though the
wind anomalies are quite similar for both GCMs, the actual structure is dissimilar: While for the MPI simulations the jet is
less constrained and deflected to the north, reaching Europe at the latitude of Ireland, the jet stream in the AWI GCM reaches
Europe at the latitude of the Iberian Peninsula and France and extends farther into the continent. In general, the simulated
winds speeds at 300 hPa in the AWI model are weaker compared to the MPI model (not shown). The zonal structure of the
wind speed anomalies identified for the AWI simulations is more similar to the ensemble mean of CMIP5 models (e.g., Ludwig
et al., 2016) than the MPI anomaly pattern.

3.2 Climate of the Regional Simulations

Based on the GCM simulations, we obtain two different variants of the regional LGM climate in western Europe. The results
are shown primarily for the larger domain of the regional simulations, as the climate of the high resolution simulations yields
a similar structure.

The annual mean 2 m air temperature is considerably lower in the WRF-MPI than in the WRF-AWI simulation (c.f. Fig. 3).
The biggest differences are identified near the ice sheet margin, with almost 10 °C in annual mean. The sign and pattern of
the differences are visible in all seasons, but winter air temperatures clearly diverge most. For the summer, air temperatures in
both models are more similar to each other. These differences can be partly attributed to the snow cover: Except for summer,
almost the entire region is covered by snow in WRF-MPI, even though a snow height of several metres is only reached over
the FIS and the Alpine region (not shown). WRF-AWI shows markedly higher snow accumulation over the ice sheets with
differences of more than 20 m compared to the WRF-MPI simulation, but generally less snow cover in southern and Central
Europe. Differences amount to 20 % less snow cover in WRF-AWI in annual mean and to 40 % in both spring and winter.
In summer, only the ice sheets are snow covered in both simulations, and the differences are thus negligible. Nevertheless,

190   more precipitation is simulated over Europe in the WRF-AWI simulation (c.f. Fig. 4). High precipitation amounts are either orographically induced as for precipitation over the Alps and over the FIS or they are associated with the moisture availability of the North Atlantic.

The absolute annual mean wind field and the associated differences are depicted in Fig. 5. Both simulations show strongest winds south of the FIS, but with a notably enhanced pattern in WRF-MPI. In contrast, westerly winds from the North Atlantic

195   are stronger in WRF-AWI, thus transporting heat and moisture towards Europe. During winter, the westerly winds are directed towards the centre of the domain in WRF-AWI, whereas in WRF-MPI the winds have a more northwestern component, directed towards the outside of the domain. In summer, both WRF-MPI and WRF-AWI simulations are charaterized by westerly winds from the North Atlantic. Again, winds from the FIS are blowing south- and southeastwards, but the summer wind speeds are consistently weaker than in winter for both simulations. These wind fields are induced by the large-scale circulation in the

200   global forcing simulations. In fact, the northerly and easterly components are predominant in the MPI simulation (Ludwig et al., 2016), whereas southerly and westerly components occur more often in the AWI simulation. This is in accordance with the jet structure in both global simulations. As the influence of the ice sheet is higher in the (global and regional) MPI simulations, this is consistent with a partially drier and generally colder climate in western Europe during LGM.

3.3   Permafrost and Ground Cracking Distribution

205   The permafrost distribution of the global and regional simulations based on the SFI is depicted in Fig. 6. The permafrost extent based on the AWI-ESM and WRF-AWI simulations does not reach farther south than the ice sheet, apart from the Alps in WRF-AWI. A modest increase in the permafrost area is simulated by the global MPI simulation. Here continuous permafrost is still limited to the ice sheet, but sporadic permafrost is slightly more widespread. The WRF-MPI simulation shows a larger permafrost extent. In eastern Europe, the distribution of ice wedge pseudomorphs (Isarin et al., 1998) strictly overlaps that of

210   modelled continuous permafrost in the third layer with a representative depth of 70 cm. In western Europe, field evidence for permafrost exceeds the modeled sporadic permafrost to the south. The conditions for discontinuous and sporadic permafrost are rarely fulfilled in all simulations.

The results of the direct method (c.f. Fig. S3) using long-term mean annual soil temperatures agree with the permafrost extent based on the SFI. However, the different types of permafrost cannot be distinguished by this method, leading to a permafrost

215   line that corresponds to that of the sporadic permafrost based on the SFI.

Permafrost estimations based on MAAT are limited to the permanent ice areas during the LGM in all four simulations (c.f. Fig. S4). Despite of the different regional climate, the hereby reconstructed permafrost boundaries closely resemble each other. The regional climate model simulations show some additional permafrost areas, which are related to higher orography, especially at the Alps, and, in WRF-MPI, also at the Pyrenees and the Massif Central (c.f. Fig. 1 and Fig. S2). These mountainous

220   areas are not adequately resolved in the global forcing simulations because of the coarse horizontal grid spacing.

Conditions for thermal contraction cracking after Matsuoka et al. (2018) have been tested based on the global and regional climate model data. Examples of how the soil temperature and the gradient develop over two consecutive years in France (locations A and B of Fig. 1) are shown in Fig. 7. Time series of the entire simulation periods for these locations can be found in

Fig. S5. The two criteria (a) ground temperature at -1 m below -5 °C and (b) temperature gradient in the upper meter of ground

225 greater than -7°C m^{-1}) are fulfilled when both curves reach below the depicted reference line. In the WRF-MPI simulation (Fig. 7 a and c), this is the case several times in both years and locations, but not in the WRF-AWI simulation.

For each grid cell, the number of days per year when the thermal contraction cracking criteria (Matsuoka et al., 2018) are fulfilled, is translated into heat maps for each simulation. The results are shown in Fig. 8. Whereas the permafrost area is much smaller in the global models than their respective regional counterpart, the opposite is the case for thermal contraction

230 cracking areas. The global AWI simulation almost meets the boundaries of sand wedge occurrence. According to the global MPI simulation, thermal contraction cracking would have been possible as far south as the Iberian Peninsula, where no field evidence for it has been found so far. This can be associated with the lower resolution of the global simulations. Here, the Pyrenees are not resolved adequately in the model and do not act as a natural barrier for cold air arriving from the North, which can thus reach further south in the GCMs (c.f. Fig. 1 and Fig. S2). As for the permafrost distribution, also the possible thermal

235 contraction cracking occurrence is poorly represented in WRF-AWI and is not able to explain the occurrence of wedges in mid and southern France. By contrast, the WRF-MPI simulation agrees well with proxy evidence. Apart from two sand wedges in the lower Rhône valley, the conditions for thermal contraction cracking are found in the simulation in the area where the features are found. This spatial coherence is further improved in the high-resolution simulation (c.f. Fig. 8 e), which can be primarily attributed to a higher resolved orography (c.f. Fig. 1 b).

240 ## 4 Summary and Discussion

In this study we explore the benefit of using regional climate model data for the delimitation of the LGM permafrost distribution in comparison with field proxies in France. The main findings can be summarized as follows.

(1) The SFI is suitable to infer LGM permafrost from climate model data. The results based on the SFI are supported by the direct method as the boundaries between permafrost occurrence and absence as indicated by the SFI fully match the permafrost

245 border derived from the annual mean ground temperature. Among the models used, the SFI based permafrost extent of the regional WRF-MPI simulation best agrees with proxy data and is clearly improved over its global counterpart.

(2) The thermal contraction cracking may have occurred much further south than the simulated permafrost limits, in a context of low and sparse vegetation. The southern extent of sand wedges in France as delineated by Andrieux et al. (2016b) fits well with the boundary of LGM thermal contraction cracking derived from the regional WRF-MPI simulation. In contrast, the

250 global MPI simulation does not resolve orographic features (e.g. the Pyrenees and the Rhone valley) sufficiently, leading to a possible southward airflow transporting cold air across France to Spain, and allows ground cracking to occur at excessively low latitudes.

(3) The obtained estimates for the possible location of permafrost is consistent with the hypothesis proposed by Andrieux et al. (2016b, 2018), who suggest that sand wedges did not exclusively form in permafrost areas during the LGM, but also developed

255 within deep seasonally frozen ground. Because thermal contraction cracking of the ground was not the limiting factor for ice wedge development during the LGM as it is today in densely vegetated Arctic areas, ice wedges would have developed in the

discontinuous and sporadic permafrost zone, with the limiting factor being only the ability for ice to be preserved from year to year. The regional WRF-MPI simulations best match the proxy-based permafrost reconstruction. The agreement with the proxies is better in eastern Europe, even though the availability of field data remains scarce in that region compared to western

260 Europe. The presence of ice wedge pseudomorphs in northern France actually shows that permafrost must have extended at least 150 km further south than simulations suggest.

The consideration of two global models enables the quantification of uncertainties associated with the large-scale flow considitions under LGM. The global MPI and AWI simulations differ in their atmospheric flow and jet structure. In AWI, the westerly flow dominates so that moisture and heat is transported from the North Atlantic towards Europe. This large-scale circulation is

265 in good agreement with the multi-model mean of the CMIP5/PMIP3 and CMIP6/PMIP4 models, whereas the MPI simulation exhibits a more northward jet stream and suggests a stronger ice sheet influence through prevailing north- and northeasterly winds (Kageyama et al., 2021; Ludwig et al., 2016). Considering that the regional WRF-MPI simulation is largely in agreement with proxy evidence for both the permafrost and ground cracking extent, we assume that the large-scale circulation of the LGM is reflected more accurately in this simulation. For wind and air pressure so far only indirect proxy evidences exist, e.g., the

270 reconstruction of easterly wind directions from sediments across the European loess belt (Dietrich and Seelos, 2010; Krauß et al., 2016; Römer et al., 2016). Because of the drier conditions with less vegetation and higher wind speeds, dust events occurred frequently during the LGM. This is reflected by the thick loess deposits in western and Central Europe, which form the European less belt (e.g., Lehmkuhl et al., 2016). Recent studies similarly support the hypothesis that, besides individual cyclone events, easterly winds induced by a semi-permanent anticyclone over the FIS were an important component for the

275 glacial dust cycle (e.g., Raible et al., 2020; Schaffernicht et al., 2020; Stevens et al., 2020).

Overall, the new regional climate simulations largely reconcile the field data and enables the reconsideration of the significance of ice wedge pseudomorphs and sand wedge casts for understanding past climate variations. Field data still suggest a wider extension of permafrost in western Europe than shown by the simulations, however, analysing the southern extent of thermal contraction cracking completes the picture. Various factors may account for a remaining gap between proxy and model data.

280 These factors include:

(1) Thermal offsets due to ground thermal conductivity (particularly the ration between conductivities in unfrozen and frozen state) may be responsible for slightly colder ground temperature in fine-grained soils (e.g., loess), although this effect is assumed to have been minor.

(2) Data from loess sections in northern France (Antoine et al., 2003, 2014) and Germany (Meszner et al., 2013) show that the

285 main phases of ice wedge development occurred between 30 ka and 24 ka. This period called the Last Permafrost Maximum (LPM, Vandenberghe et al., 2014) covers short and very cold events, which resulted in wider permafrost extension than during the LGM sensu stricto. However, boundary conditions for the simulations are only known accurately at 21 ka.

To conclude, the combination of the well established permafrost index SFI and the criteria for thermal contraction cracking by Matsuoka et al. (2018), both based on regional climate model data, provides new possibilities for the estimation of the

290 permafrost extent and the interpretation of ice and sand wedges, especially for paleoclimate applications. In this context, the

use of regional climate model simulations with a highly resolved orography is clearly beneficial and should be considered for other regions than western Europe.

Author contributions. PL, PB and JGP designed the concept of the study. PL adjusted the WRF model for LGM applications. KHA performed the regional simulations with the WRF model, analysed the data and created the figures. XS and GL provided data of the global AWI simulations. PB provided the proxy data. KHA wrote the first draft of the manuscript. All authors contributed with discussions and revisions to the final manuscript.

References

Andrieux, E., Bertran, P., Antoine, P., Deschodt, L., Lenoble, A., Coutard, S., Ajas, A., Borderie, Q., Coutard, J.-P., Didierjean, F., et al.: Database of pleistocene periglacial featuresin France: description of the online version, Quaternaire. Revue de l'Association française pour l'étude du Quaternaire, 27, 329–339, https://doi.org/https://doi.org/10.4000/quaternaire.7717, 2016a.

315 Andrieux, E., Bertran, P., and Saito, K.: Spatial analysis of the French Pleistocene permafrost by a GIS database, Permafrost and Periglacial Processes, 27, 17–30, https://doi.org/10.1002/ppp.1856, 2016b.

Andrieux, E., Bateman, M. D., and Bertran, P.: The chronology of Late Pleistocene thermal contraction cracking derived from sand wedge OSL dating in central and southern France, Permafrost and Periglacial Processes, 162, 84–100, http://www.sciencedirect.com/science/article/pii/S0921818117302370, 2018.

320 Annan, J. D. and Hargreaves, J. C.: A new global reconstruction of temperature changes at the Last Glacial Maximum, Climate of the Past, 9, 367–376, https://doi.org/10.5194/cp-9-367-2013, 2013.

Antoine, P., Catt, J., Lautridou, J.-P., and Sommé, J.: The loess and coversands of northern France and southern England, Journal of Quaternary Science, 18, 309–318, https://doi.org/https://doi.org/10.1002/jqs.750, 2003.

Antoine, P., Rousseau, D.-D., Moine, O., Kunesch, S., Hatté, C., Lang, A., Tissoux, H., and Zöller, L.: Rapid and cyclic aeolian deposition
325 during the Last Glacial in European loess: a high-resolution record from Nussloch, Germany, Quaternary Science Reviews, 28, 2955–2973, https://doi.org/https://doi.org/10.1016/j.quascirev.2009.08.001, 2009.

Antoine, P., Goval, E., Jamet, G., Coutard, S., Moine, O., Hérisson, D., Auguste, P., Guérin, G., Lagroix, F., Schmidt, E., Robert, V., Debenham, N., Meszner, S., and Bahain, J.-J.: Les séquences loessiques pléistocène supérieur d'Havrincourt (Pas-de-Calais, France) : stratigraphie, paléoenvironnements, géochronologie et occupations paléolithiques, Quaternaire, 25, 321–368,
330 https://doi.org/10.4000/quaternaire.7278, 2014.

Barosh, P. J.: Frostquakes in New England, Engineering geology, 56, 389–394, 2000.

Bartlein, P. J., Harrison, S. P., Brewer, S., Connor, S., Davis, B. A. S., Gajewski, K., Guiot, J., Harrison-Prentice, T. I., Henderson, A., Peyron, O., Prentice, I. C., Scholze, M., Seppä, H., Shuman, B., Sugita, S., Thompson, R. S., Viau, A. E., Williams, J., and Wu, H.: Pollen-based continental climate reconstructions at 6 and 21 ka: a global synthesis, Climate Dynamics, 37, 775–802, https://doi.org/10.1007/s00382-
335 010-0904-1, 2011.

Bertran, P., Andrieux, E., Antoine, P., Coutard, S., Deschodt, L., Gardère, P., Hernandez, M., Legentil, C., Lenoble, A., Liard, M., Mercier, N., Moine, O., Sitzia, L., and Van Vliet-Lanoë, B.: Distribution and chronology of Pleistocene permafrost features in France: Database and first results, Boreas, 43, 699–711, https://doi.org/10.1111/bor.12025, 2014.

Bockheim, J. G., Kurz, M. D., Soule, S. A., and Burke, A.: Genesis of active sand-filled polygons in lower and central Beacon Valley,
340 Antarctica, Permafrost and Periglacial Processes, 20, 295–308, 2009.

Braconnot, P., Harrison, S., Kageyama, M., Bartlein, P., Masson-Delmotte, V., Abe-Ouchi, A., Otto-Bliesner, B., and Zhao, Y.: Evaluation of climate models using palaeoclimate data, Nature Climate Change, 2, 417–424, https://doi.org/10.1038/NCLIMATE1456, 2012.

Brierley, C. M., Zhao, A., Harrison, S. P., Braconnot, P., Williams, C. J. R., Thornalley, D. J. R., Shi, X., Peterschmitt, J.-Y., Ohgaito, R., Kaufman, D. S., Kageyama, M., Hargreaves, J. C., Erb, M. P., Emile-Geay, J., D'Agostino, R., Chandan, D., Carré, M., Bartlein,
345 P. J., Zheng, W., Zhang, Z., Zhang, Q., Yang, H., Volodin, E. M., Tomas, R. A., Routson, C., Peltier, W. R., Otto-Bliesner, B., Morozova, P. A., McKay, N. P., Lohmann, G., Legrande, A. N., Guo, C., Cao, J., Brady, E., Annan, J. D., and Abe-Ouchi, A.: Large-scale features and

evaluation of the PMIP4-CMIP6 *midHolocene* simulations, Climate of the Past, 16, 1847–1872, https://doi.org/10.5194/cp-16-1847-2020, 2020.

Burn, C. R.: Implications for palaeoenvironmental reconstruction of recent ice-wedge development at Mayo, Yukon Territory, Permafrost

350   and Periglacial Processes, 1, 3–14, 1990.

Clark, P. U., Dyke, A. S., Shakun, J. D., Carlson, A. E., Clark, J., Wohlfarth, B., Mitrovica, J. X., Hostetler, S. W., and McCabe, A. M.: The Last Glacial Maximum, Science, 325, 710–714, https://doi.org/10.1126/science.1172873, 2009.

Cleator, S. F., Harrison, S. P., Nichols, N. K., Prentice, I. C., and Roulstone, I.: A new multivariable benchmark for Last Glacial Maximum climate simulations, Climate of the Past, 16, 699–712, https://doi.org/10.5194/cp-16-699-2020, 2020.

355   CLIMAP Project Members: The last interglacial ocean, Quat. Res., 2, 123–224, https://doi.org/doi:10.1016/0033-5894(84)90098-X, 1984.

Dietrich, S. and Seelos, K.: The reconstruction of easterly wind directions for the Eifel region (Central Europe) during the period 40.3-12.9 ka BP, Climate of the Past, 6, 145–154, https://doi.org/10.5194/cp-6-145-2010, 2010.

Eyring, V., Bony, S., Meehl, G. A., Senior, C. A., Stevens, B., Stouffer, R. J., and Taylor, K. E.: Overview of the Coupled Model Intercomparison Project Phase 6 (CMIP6) experimental design and organization, Geoscientific Model Development, 9, 1937–1958,

360   https://doi.org/10.5194/gmd-9-1937-2016, 2016.

Flückiger, J., Knutti, R., White, J. W. C., and Renssen, H.: Modeled seasonality of glacial abrupt climate events, Climate Dynamics, 31, 633–645, https://doi.org/10.1007/s00382-008-0373-y, 2008.

Fortier, D. and Allard, M.: Frost-cracking conditions, Bylot Island, eastern Canadian Arctic archipelago, Permafrost and Periglacial Processes, 16, 145–161, https://doi.org/10.1002/ppp.504, 2005.

365   Frauenfeld, O. W., Zhang, T., and Mccreight, J. L.: Northern Hemisphere freezing/thawing index variations over the twentieth century, International Journal of Climatology, 27, 47–63, https://doi.org/10.1002/joc.1372, 2007.

Harris, C., Arenson, L. U., Christiansen, H. H., Etzelmüller, B., Frauenfelder, R., Gruber, S., Haeberli, W., Hauck, C., Hölzle, M., Humlum, O., Isaksen, K., Kääb, A., Kern-Lütschg, M. A., Lehning, M., Matsuoka, N., Murton, J. B., Nötzli, J., Phillips, M., Ross, N., Seppälä, M., Springman, S. M., and Vonder Mühll, D.: Permafrost and climate in Europe: Monitoring and modelling thermal, geomorphological and

370   geotechnical responses, Earth-Science Reviews, 92, 117 – 171, https://doi.org/https://doi.org/10.1016/j.earscirev.2008.12.002, 2009.

Harrison, S. P., Bartlein, P. J., Izumi, K., Li, G., Annan, J., Hargreaves, J., P., B., and Kageyama, M.: Evaluation of CMIP5 palaeo-simulations to improve climate projections, Nature Climate Change, 5, 735–743, https://doi.org/10.1038/nclimate2649, 2015.

Hatté, C., Fontugne, M., Rousseau, D.-D., Antoine, P., Zöller, L., Laborde, N. T., and Bentaleb, I.: δ13C variations of loess organic matter as a record of the vegetation response to climatic changes during the Weichselian, Geology, 26, 583–586, https://doi.org/10.1130/0091-

375   7613(1998)026<0583:CVOLOM>2.3.CO;2, 1998.

Hatté, C., Antoine, P., Fontugne, M., Lang, A., Rousseau, D.-D., and Zöller, L.: δ13C of Loess Organic Matter as a Potential Proxy for Paleoprecipitation, Quaternary Research, 55, 33–38, https://doi.org/https://doi.org/10.1006/qres.2000.2191, 2001.

Hong, S.-Y., Dudhia, J., and Chen, S.-H.: A Revised Approach to Ice Microphysical Processes for the Bulk Parameterization of Clouds and Precipitation, Monthly Weather Review, 132, 103–120, https://doi.org/10.1175/1520-0493(2004)132<0103:ARATIM>2.0.CO;2, 2004.

380   Hong, S.-Y., Noh, Y., and Dudhia, J.: A New Vertical Diffusion Package with an Explicit Treatment of Entrainment Processes, Monthly Weather Review, 134, 2318–2341, https://doi.org/10.1175/MWR3199.1, 2006.

Hughes, A. L. C., Gyllencreutz, R., Lohne, O. S., Mangerud, J., and Svendsen, J. I.: The last Eurasian ice sheets – a chronological database and time-slice reconstruction, DATED-1, Boreas, 45, 1–45, https://doi.org/https://doi.org/10.1111/bor.12142, 2015.

Iacono, M. J., Delamere, J. S., Mlawer, E. J., Shephard, M. W., Clough, S. A., and Collins, W. D.: Radiative forcing by long-
385   lived greenhouse gases: Calculations with the AER radiative transfer models, Journal of Geophysical Research: Atmospheres, 113,
       https://doi.org/10.1029/2008JD009944, 2008.

IPCC: Climate Change 2013: The Physical Science Basis. Contribution of Working Group I to the Fifth Assessment Report of the Intergov-
       ernmental Panel on Climate Change, stocker, T.F., D. Qin, G.-K. Plattner, M. Tignor, S.K. Allen, J. Boschung, A. Nauels, Y. Xia, V. Bex
       and P.M. Midgley (eds.). Cambridge University Press, Cambridge, United Kingdom and New York, NY, USA, 2013.

390   IPCC: IPCC Special Report on the Ocean and Cryosphere in a Changing Climate, po¨rtner, H.-O., Roberts, D.C., Masson-Delmotte, V., Zhai,
       P., Tignor, M., Poloczanska, E., Mintenbeck, K., Alegri´a, A., Nicolai, M., Okem, A., Petzold, J., Rama, B. and Weyer, N.M. (eds.). In
       press, 2019.

Isarin, R. F. B., Renssen, H., and Vandenberghe, J.: The impact of the North Atlantic Ocean on the Younger Dryas climate in northwest-
       ern and central Europe, Journal of Quaterny Science, 13, 447–453, https://doi.org/10.1002/(SICI)1099-1417(1998090)13:5<447::AID-
395   JQS402>3.0.CO;2-B, 1998.

Jiménez, P. A., Dudhia, J., González-Rouco, J. F., Navarro, J., Montávez, J. P., and García-Bustamante, E.: A Revised Scheme for the WRF
       Surface Layer Formulation, Monthly Weather Review, 140, 898–918, https://doi.org/10.1175/MWR-D-11-00056.1, 2012.

Jungclaus, J., Giorgetta, M., Reick, C., Legutke, S., Brovkin, V., Crueger, T., Esch, M., Fieg, K., Fischer, N., Glushak, K., Gayler, V., Haak,
       H., Hollweg, H.-D., Kinne, S., Kornblueh, L., Matei, D., Mauritsen, T., Mikolajewicz, U., Müller, W., Notz, D., Pohlmann, T., Raddatz,
400   T., Rast, S., Roeckner, E., Salzmann, M., Schmidt, H., Schnur, R., Segschneider, J., Six, K., Stockhause, M., Wegner, J., Widmann, H.,
       Wieners, K.-H., Claussen, M., Marotzke, J., and Stevens, B.: CMIP5 simulations of the Max Planck Institute for Meteorology (MPI-M)
       based on the MPI-ESM-P model: The lgm experiment, served by ESGF, https://doi.org/10.22033/ESGF/CMIP6.9330, 2012a.

Jungclaus, J., Giorgetta, M., Reick, C., Legutke, S., Brovkin, V., Crueger, T., Esch, M., Fieg, K., Fischer, N., Glushak, K., Gayler, V., Haak,
       H., Hollweg, H.-D., Kinne, S., Kornblueh, L., Matei, D., Mauritsen, T., Mikolajewicz, U., Müller, W., Notz, D., Pohlmann, T., Raddatz,
405   T., Rast, S., Roeckner, E., Salzmann, M., Schmidt, H., Schnur, R., Segschneider, J., Six, K., Stockhause, M., Wegner, J., Widmann, H.,
       Wieners, K.-H., Claussen, M., Marotzke, J., and Stevens, B.: CMIP5 simulations of the Max Planck Institute for Meteorology (MPI-M)
       based on the MPI-ESM-P model: The lgm experiment, served by ESGF, https://doi.org/10.1594/WDCC/CMIP5.MXEPpc, 2012b.

Jungclaus, J. H., Fischer, N., Haak, H., Lohmann, K., Marotzke, J., Matei, D., Mikolajewicz, U., Notz, D., and von Storch, J. S.: Character-
       istics of the ocean simulations in the Max Planck Institute Ocean Model (MPIOM) the ocean component of the MPI-Earth system model,
410   Journal of Advances in Modeling Earth Systems, 5, 422–446, https://doi.org/10.1002/jame.20023, 2013.

Justino, F. and Peltier, W. R.: The glacial North Atlantic Oscillation, Geophysical Research Letters, 32,
       https://doi.org/10.1029/2005GL023822, 2005.

Kageyama, M., Albani, S., Braconnot, P., Harrison, S. P., Hopcroft, P. O., Ivanovic, R. F., Lambert, F., Marti, O., Peltier, W. R., Peterschmitt,
       J.-Y., Roche, D. M., Tarasov, L., Zhang, X., Brady, E. C., Haywood, A. M., LeGrande, A. N., Lunt, D. J., Mahowald, N. M., Mikolajew-
415   icz, U., Nisancioglu, K. H., Otto-Bliesner, B. L., Renssen, H., Tomas, R. A., Zhang, Q., Abe-Ouchi, A., Bartlein, P. J., Cao, J., Li, Q.,
       Lohmann, G., Ohgaito, R., Shi, X., Volodin, E., Yoshida, K., Zhang, X., and Zheng, W.: The PMIP4 contribution to CMIP6 – Part 4: Sci-
       entific objectives and experimental design of the PMIP4-CMIP6 Last Glacial Maximum experiments and PMIP4 sensitivity experiments,
       Geoscientific Model Development, 10, 4035–4055, https://doi.org/10.5194/gmd-10-4035-2017, 2017.

Kageyama, M., Harrison, S. P., Kapsch, M.-L., Lofverstrom, M., Lora, J. M., Mikolajewicz, U., Sherriff-Tadano, S., Vadsaria, T., Abe-Ouchi,
420   A., Bouttes, N., Chandan, D., Gregoire, L. J., Ivanovic, R. F., Izumi, K., LeGrande, A. N., Lhardy, F., Lohmann, G., Morozova, P. A.,
       Ohgaito, R., Paul, A., Peltier, W. R., Poulsen, C. J., Quiquet, A., Roche, D. M., Shi, X., Tierney, J. E., Valdes, P. J., Volodin, E., and Zhu,

J.: The PMIP4 Last Glacial Maximum experiments: preliminary results and comparison with the PMIP3 simulations, Climate of the Past, 17, 1065–1089, https://doi.org/10.5194/cp-17-1065-2021, 2021.

Kain, J. S.: The Kain–Fritsch Convective Parameterization: An Update, Journal of Applied Meteorology, 43, 170–181,
425   https://doi.org/10.1175/1520-0450(2004)043<0170:TKCPAU>2.0.CO;2, 2004.

Keeble, J., Hassler, B., Banerjee, A., Checa-Garcia, R., Chiodo, G., Davis, S., Eyring, V., Griffiths, P. T., Morgenstern, O., Nowack, P., Zeng, G., Zhang, J., Bodeker, G., Burrows, S., Cameron-Smith, P., Cugnet, D., Danek, C., Deushi, M., Horowitz, L. W., Kubin, A., Li, L., Lohmann, G., Michou, M., Mills, M. J., Nabat, P., Olivié, D., Park, S., Seland, Ø., Stoll, J., Wieners, K.-H., and Wu, T.: Evaluating stratospheric ozone and water vapour changes in CMIP6 models from 1850 to 2100, Atmospheric Chemistry and Physics, 21, 5015–5061,
430   https://doi.org/10.5194/acp-21-5015-2021, 2021.

Kitover, D. C., van Balen, R. T., Roche, D. M., Vandenberghe, J., and Renssen, H.: New Estimates of Permafrost Evolution during the Last 21 k Years in Eurasia using Numerical Modelling, Permafrost and Periglacial Processes, 24, 286–303, https://doi.org/10.1002/ppp.1787, 2013.

Kokelj, S., Lantz, T., Wolfe, S. A., Kanigan, J., Morse, P., Coutts, R., Molina-Giraldo, N., and Burn, C. R.: Distribution and activity of
435   ice wedges across the forest-tundra transition, western Arctic Canada, Journal of Geophysical Research: Earth Surface, 119, 2032–2047, 2014.

Krauß, L., Zens, J., Zeeden, C., Schulte, P., Eckmeier, E., and Lehmkuhl, F.: A Multi-Proxy Analysis of two Loess-Paleosol Sequences in the Northern Harz Foreland, Germany, Palaeogeography, Palaeoclimatology, Palaeoecology, 461, 401–417, https://doi.org/https://doi.org/10.1016/j.palaeo.2016.09.001, 2016.

440   Lambeck, K., Yokoyama, Y., and Purcell, T.: Into and out of the Last Glacial Maximum: sea-level change during Oxygen Isotope Stages 3 and 2, Quaternary Science Reviews, 21, 343 – 360, https://doi.org/https://doi.org/10.1016/S0277-3791(01)00071-3, ePILOG, 2002.

Lambeck, K., Rouby, H., Purcell, A., Sun, Y., and Sambridge, M.: Sea level and global ice volumes from the Last Glacial Maximum to the Holocene, Proceedings of the National Academy of Sciences, 111, 15 296–15 303, 2014.

Lehmkuhl, F., Zens, J., Krauß, L., Schulte, P., and Kels, H.: Loess-paleosol sequences at the northern European
445   loess belt in Germany: Distribution, geomorphology and stratigraphy, Quaternary Science Reviews, 153, 11 – 30, https://doi.org/https://doi.org/10.1016/j.quascirev.2016.10.008, 2016.

Levavasseur, G., Vrac, M., Roche, D., Paillard, D., Martin, A., and Vandenberghe, J.: Present and LGM permafrost from climate simulations : contribution of statistical downscaling, Climate of the Past, 7, 1225–1246, https://doi.org/10.5194/cp-7-1225-2011, 2011.

Levy, J. S., Head, J. W., and Marchant, D. R.: The role of thermal contraction crack polygons in cold-desert fluvial systems, Antarctic
450   Science, 20, 565, 2008.

Li, C. and Battisti, D. S.: Reduced Atlantic Storminess during Last Glacial Maximum: Evidence from a Coupled Climate Model, Journal of Climate, 21, 3561–3579, https://doi.org/10.1175/2007JCLI2166.1, 2008.

Liu, Y. and Jiang, D.: Last glacial maximum permafrost in China from CMIP5 simulations, Palaeogeography, Palaeoclimatology, Palaeoecology, 447, 12–21, https://doi.org/10.1016/j.palaeo.2016.01.042, 2016a.

455   Liu, Y. and Jiang, D.: Mid-Holocene permafrost: Results from CMIP5 simulations, Journal of Geophysical Research: Atmospheres, 121, 221–240, https://doi.org/10.1002/2015JD023837, 2016b.

Lohmann, G., Butzin, M., Eissner, N., Shi, X., and Stepanek, C.: Abrupt Climate and Weather Changes Across Time Scales, Paleoceanography and Paleoclimatology, 35, e2019PA003 782, https://doi.org/https://doi.org/10.1029/2019PA003782, e2019PA003782 10.1029/2019PA003782, 2020.

460 Ludwig, P., Schaffernicht, E. J., Shao, Y., and Pinto, J. G.: Regional atmospheric circulation over Europe during the Last Glacial Maximum
and its links to precipitation, Journal of Geophysical Research: Atmospheres, 121, 2130–2145, https://doi.org/10.1002/2015JD024444,
2016.

Ludwig, P., Pinto, J. G., Raible, C. C., and Shao, Y.: Impacts of surface boundary conditions on regional climate model simulations of European climate during the Last Glacial Maximum, Geophysical Research Letters, 44, 5086–5095, https://doi.org/10.1002/2017GL073622,
465 2017.

Ludwig, P., Gómez-Navarro, J. J., Pinto, J. G., Raible, C. C., Wagner, S., and Zorita, E.: Perspectives of regional paleoclimate modeling,
Annals of the New York Academy of Sciences, 1436, 54–69, https://doi.org/https://doi.org/10.1111/nyas.13865, 2019.

Löfverström, M., Caballero, R., Nilsson, J., and Kleman, J.: Evolution of the large-scale atmospheric circulation in response to changing ice
sheets over the last glacial cycle, Climate of the Past, 10, 1453–1471, https://doi.org/10.5194/cp-10-1453-2014, 2014.

470 Mackay, J. R. and Burn, C. R.: The first 20 years (1978-1979 to 1998-1999) of active-layer development, Illisarvik experimental drained lake
site, western Arctic coast, Canada1, Canadian Journal of Earth Sciences, 39, 1657–1674, 2002.

MARGO Project Members: Constraints on the magnitude and patterns of ocean cooling at the Last Glacial Maximum, Nature Geoscience,
2, 127–132, https://doi.org/doi:10.1038/ngeo411, 2009.

Marsland, S. J., Haak, H., Jungclaus, J. H., Latif, M., and Röske, F.: The Max-Planck-Institute global ocean/sea ice model with orthogonal
475 curvilinear coordinates, Ocean Modelling, 5, 91 – 127, https://doi.org/https://doi.org/10.1016/S1463-5003(02)00015-X, 2003.

Matsuoka, N., Christiansen, H. H., and Watanabe, T.: Ice-wedge polygon dynamics in Svalbard: Lessons from a decade of automated multi-sensor monitoring, Permafrost and Periglacial Processes, 29, 210–227, https://doi.org/10.1002/ppp.1985, 2018.

Merz, N., Raible, C. C., and Woollings, T.: North Atlantic Eddy-Driven Jet in Interglacial and Glacial Winter Climates, Journal of Climate,
28, 3977–3997, https://doi.org/10.1175/JCLI-D-14-00525.1, 2015.

480 Meszner, S., Kreutzer, S., Fuchs, M., and Faust, D.: Late Pleistocene landscape dynamics in Saxony, Germany: Paleoenvironmental reconstruction using loess-paleosol sequences, Quaternary International, 296, 94–107,
https://doi.org/https://doi.org/10.1016/j.quaint.2012.12.040, closing the gap - North Carpathian loess traverse in the Eurasian loess
belt 6th Loess Seminar, Wrocław, Poland Dedicated to Prof. Henryk Maruszczak, 2013.

Mix, A. C., Bard, E., and Schneider, R.: Environmental processes of the ice age: land, oceans, glaciers (EPILOG), Quaternary Science
485 Reviews, 20, 627 – 657, https://doi.org/https://doi.org/10.1016/S0277-3791(00)00145-1, 2001.

Monnin, E., Indermühle, A., Dällenbach, A., Flückiger, J., Stauffer, B., Stocker, T. F., Raynaud, D., and Barnola, J.-M.: Atmospheric CO2
Concentrations over the Last Glacial Termination, Science, 291, 112–114, https://doi.org/10.1126/science.291.5501.112, 2001.

Murton, J. B.: Permafrost and Periglacial Features. Ice wedges and ice wedge casts, in: Encyclopedia of Quaternary Science, edited by Elias,
S. A., vol. 2, pp. 436 – 451, Elsevier, Amsterdam, 2013.

490 Nelson, F. E. and Outcalt, S. I.: A Computational Method for Prediction and Regionalization of Permafrost, Arctic and Alpine Research, 19,
279–288, https://doi.org/10.1080/00040851.1987.12002602, 1987.

Okkonen, J., Neupauer, R., Kozlovskaya, E., Afonin, N., Moisio, K., Taewook, K., and Muurinen, E.: Frost Quakes: Crack Formation by
Thermal Stress, Journal of Geophysical Research: Earth Surface, 125, e2020JF005 616, 2020.

Pausata, F. S. R., Li, C., Wettstein, J., Kageyama, M., and Nisancioglu, K.: The key role of topography in altering North Atlantic atmospheric
495 circulation during the last glacial period, Climate of the Past, 7, https://doi.org/10.5194/cp-7-1089-2011, 2011.

Peltier, W. R., Argus, D. F., and Drummond, R.: Space geodesy constrains ice age terminal deglaciation: The global ICE-6G_C (VM5a)
model, Journal of Geophysical Research: Solid Earth, 120, 450–487, https://doi.org/https://doi.org/10.1002/2014JB011176, 2015.

Pewe, T. L.: Sand-wedge polygons (tesselations) in the McMurdo Sound region, Antarctica; a progress report, American Journal of Science, 257, 545–552, 1959.

500   Péwé, T. L.: Paleoclimatic significance of fossil ice wedges, Biul. peryglac., 15, 65–73, 1966.

Pfahl, S., O'Gorman, P. A., and Singh, M. S.: Extratropical Cyclones in Idealized Simulations of Changed Climates, Journal of Climate, 28, 9373–9392, https://doi.org/10.1175/JCLI-D-14-00816.1, 2015.

Pinto, J. G. and Ludwig, P.: Extratropical cyclones over the North Atlantic and western Europe during the Last Glacial Maximum and implications for proxy interpretation, Climate of the Past, 16, 611–626, https://doi.org/10.5194/cp-16-611-2020, 2020.

505   Prentice, I. C. and Harrison, S. P.: Ecosystem effects of CO_2 concentration: evidence from past climates, Climate of the Past, 5, 297–307, https://doi.org/10.5194/cp-5-297-2009, 2009.

Prospero, J. M., Ginoux, P., Torres, O., Nicholson, S. E., and Gill, T. E.: Environmental characterization of global sources of atmoshperic soil dust identified with the NIMBUS 7 total ozone mapping spectrometer (TOMS) absorbing aerosol product, Reviews of Geophysics, 40, https://doi.org/10.1029/2000RG000095, 2002.

510   Raible, C. C., Pinto, J. G., Ludwig, P., and Messmer, M.: A review of past changes in extratropical cyclones in the northern hemisphere and what can be learned for the future, WIREs Climate Change, https://doi.org/10.1002/wcc.680, 2020.

Ray, N. and Adams, J. M.: A GIS-based vegetation map of the world at the Last Glacial Maximum (25,000-15,000 BP), Internet Archaeology, 11, 2001.

Romanovskij, N.: Regularities in formation of frost fissures and development of frost fissure polygons, Biuletyn Peryglacjalny, 23, 237–277, 515   1973.

Römer, W., Lehmkuhl, F., and Sirocko, F.: Late Pleistocene aeolian dust provenances and wind direction changes reconstructed by heavy mineral analysis of the sediments of the Dehner dry maar (Eifel, Germany), Global and Planetary Change, 147, 25–39, https://doi.org/https://doi.org/10.1016/j.gloplacha.2016.10.012, 2016.

Saito, K., Sueyoshi, T., Marchenko, S., Romanovsky, V., Otto-Bliesner, B., Walsh, J., Bigelow, N., Hendricks, A., and Yoshikawa, K.: LGM 520   permafrost distribution: how well can the latest PMIP multi-model ensembles perform reconstruction?, Climate of the Past, 9, 1697–1714, https://doi.org/10.5194/cp-9-1697-2013, 2013.

Schaffernicht, E. J., Ludwig, P., and Shao, Y.: Linkage between dust cycle and loess of the Last Glacial Maximum in Europe, Atmospheric Chemistry and Physics, 20, 4969–4986, https://doi.org/10.5194/acp-20-4969-2020, 2020.

Schuur, E. A. G., McGuire, A. D., Schädel, C., Grosse, G., Harden, J. W., Hayes, D. J., Hugelius, G., D., K. C., Kuhry, P., Lawrence, D. M., 525   Natali, S. M., Olefeldt, D., Romanovsky, V. E., Schaefer, K., Turetsky, M. R., Treat, C. C., and Vonk, J. E.: Climate change and the permafrost carbon feedback, Nature, 520, 171–179, https://doi.org/10.1038/nature14338, 2015.

Seguinot, J., Ivy-Ochs, S., Jouvet, G., Huss, M., Funk, M., and Preusser, F.: Modelling last glacial cycle ice dynamics in the Alps, The Cryosphere, 12, 3265–3285, https://doi.org/10.5194/tc-12-3265-2018, 2018.

Sidorenko, D., Rackow, T., Semmler, T., Barbi, D., Danilov, S., Dethloff, K., Dorn, W., Fieg, K., Goessling, H. F., Handorf, D., Harig, 530   S., Hiller, W., Juricke, S., Losch, M., Schröter, J., Sein, D. V., and Wang, Q.: Towards multi-resolution global climate modeling with ECHAM6–FESOM. Part I: model formulation and mean climate, Climate Dynamics, 44, 757–780, https://doi.org/10.1007/s00382-014-2290-6, 2015.

Sima, A., Rousseau, D.-D., Kageyama, M., Ramstein, G., Schulz, M., Balkanski, Y., Antoine, P., Dulac, F., and Hatté, C.: Imprint of North-Atlantic abrupt climate changes on western European loess deposits as viewed in a dust emission model, Quaternary Science Reviews, 28, 535   2851–2866, https://doi.org/https://doi.org/10.1016/j.quascirev.2009.07.016, 2009.

Climate
of the Past
Discussions

Skamarock, W., Klemp, J., Dudhia, J., Gill, D., Barker, D., Duda, M., Huang, X.-Y., Wang, W., and Powers, J.: A description of the advanced research WRF version 3, NCAR Tech. Note NCAR/TN-475+STR, 113, https://doi.org/10.5065/D68S4MVH, 2008.

Slater, A. G. and Lawrence, D. M.: Diagnosing Present and Future Permafrost from Climate Models, Journal of Climate, 26, 5608–5623, https://doi.org/10.1175/JCLI-D-12-00341.1, 2013.

540   Smerdon, J. E.: Climate models as a test bed for climate reconstruction methods: pseudoproxy experiments, WIREs Climate Change, 3, 63–77, https://doi.org/https://doi.org/10.1002/wcc.149, 2012.

Smith, M. and Riseborough, D.: Climate and the limits of permafrost: a zonal analysis, Permafrost and Periglacial Processes, 13, 1–15, 2002.

Stendel, M. and Christensen, J. H.: Impact of global warming on permafrost conditions in a coupled GCM, Geophysical Research Letters, 29, https://doi.org/10.1029/2001GL014345, 2002.

545   Stevens, B., Giorgetta, M., Esch, M., Mauritsen, T., Crueger, T., Rast, S., Salzmann, M., Schmidt, H., Bader, J., Block, K., Brokopf, R., Fast, I., Kinne, S., Kornblueh, L., Lohmann, U., Pincus, R., Reichler, T., and Roeckner, E.: Atmospheric component of the MPI-M Earth System Model: ECHAM6, Journal of Advances in Modeling Earth Systems, 5, 146–172, https://doi.org/10.1002/jame.20015, 2013.

Stevens, T., Sechi, D., Bradák, B., Orbe, R., Baykal, Y., Cossu, G., Tziavaras, C., Andreucci, S., and Pascucci, V.: Abrupt last glacial dust fall over southeast England associated with dynamics of the British-Irish ice sheet, Quaternary Science Reviews, 250, 106 641,

550   https://doi.org/https://doi.org/10.1016/j.quascirev.2020.106641, 2020.

Tarasov, L. and Peltier, R., W.: Greenland glacial history, borehole constraints, and Eemian extent, Journal of Geophysical Research: Solid Earth, 108, https://doi.org/10.1029/2001JB001731, 2003.

Taylor, K. E., Stouffer, R. J., and Meehl, G. A.: An Overview of CMIP5 and the Experiment Design, Bulletin of the American Meteorological Society, 93, 485 – 498, https://doi.org/10.1175/BAMS-D-11-00094.1, 2012.

555   Tewari, M., Chen, F., Wang, W., Dudhia, J., LeMone, M. A., Mitchell, K., Ek, M., Gayno, G., Wegiel, J., and Cuenca, R. H.: Implementation and verification of the unified NOAH land surface model in the WRF model, 20th conference on weather analysis and forecasting/16th conference on numerical weather prediction, pp. 11–15, https://www2.mmm.ucar.edu/wrf/users/phys_refs/LAND_SURFACE/noah.pdf, 2004.

Throop, J., Lewkowicz, A. G., and Smith, S. L.: Climate and ground temperature relations at sites across the continuous and discontinuous

560   permafrost zones, northern Canada, Canadian Journal of Earth Sciences, 49, 865–876, 2012.

Ullman, D. J., LeGrande, A. N., Carlson, A. E., Anslow, F. S., and Licciardi, J. M.: Assessing the impact of Laurentide Ice Sheet topography on glacial climate, Climate of the Past, 10, 487–507, https://doi.org/10.5194/cp-10-487-2014, 2014.

van Everdingen, R. O.: Multi-language glossary of permafrost and related ground-ice terms, 2005.

Vandenberghe, J., Renssen, H., Roche, D. M., Goosse, H., Velichko, A. A., Gorbunov, A., and Levavasseur, G.:

565   Eurasian permafrost instability constrained by reduced sea-ice cover, Quaternary Science Reviews, 34, 16 – 23, https://doi.org/https://doi.org/10.1016/j.quascirev.2011.12.001, 2012.

Vandenberghe, J., French, H. M., Gorbunov, A., Marchenko, S., Velichko, A. A., Jin, H., Cui, Z., Zhang, T., and Wan, X.: The Last Permafrost Maximum (LPM) map of the Northern Hemisphere: permafrost extent and mean annual air temperatures, 25–17 ka BP, Boreas, 43, 652–666, https://doi.org/10.1111/bor.12070, 2014.

570   Wang, Q., Danilov, S., Sidorenko, D., Timmermann, R., Wekerle, C., Wang, X., Jung, T., and Schröter, J.: The Finite Element Sea Ice-Ocean Model (FESOM) v.1.4: formulation of an ocean general circulation model, Geoscientific Model Development, 7, 663–693, https://doi.org/10.5194/gmd-7-663-2014, 2014.

Wang, T., Liu, Y., and Huang, W.: Last Glacial Maximum Sea Surface Temperatures: A Model-Data Comparison, Atmospheric and Oceanic Science Letters, 6, 233–239, https://doi.org/10.3878/j.issn.1674-2834.13.0019, 2013.

575　Washburn, A. L.: Frost cracking in a middle latitude climate, Biul. Peryglac., 12, 175 – 189, 1963.

Washburn, A. L.: Geocryology: a survey of periglacial processes and environments, Wiley, 1979.

Woillez, M.-N., Kageyama, M., Krinner, G., Noblet-Ducoudré, N. d., Viovy, N., and Mancip, M.: Impact of CO 2 and climate on the Last Glacial Maximum vegetation: results from the ORCHIDEE/IPSL models, Climate of the Past, 7, 557–577, 2011.

Wolfe, S. A., Morse, P. D., Neudorf, C. M., Kokelj, S. V., Lian, O. B., and O'Neill, H. B.: Contemporary sand
580　wedge development in seasonally frozen ground and paleoenvironmental implications, Geomorphology, 308, 215 – 229, https://doi.org/https://doi.org/10.1016/j.geomorph.2018.02.015, 2018.

Table 1. Physical parametrization schemes used for the regional simulations.

	WRF-namelist option	Scheme and Reference
Micro Physics	mp_physics = 4	WRF Single-moment 5-class Scheme
		Hong et al. (2004)
Radiation	ra_sw_physics = 4	rrtmg scheme
	ra_lw_physics = 4	Iacono et al. (2008)
Surface Layer	sf_sfclay_physics = 1	Revised MM5 Monin-Obukhov scheme
		Jiménez et al. (2012)
Land Surface	sf_surface_physics = 2	unified Noah Land Surface Model
		Tewari et al. (2004)
Planetary Boundary Layer	bl_pbl_physics = 1	Yonsei University Scheme (YSU scheme)
		Hong et al. (2006)
Cumulus Parametrization	cu_physics = 1	Kain-Fritsch Scheme
		Kain (2004)
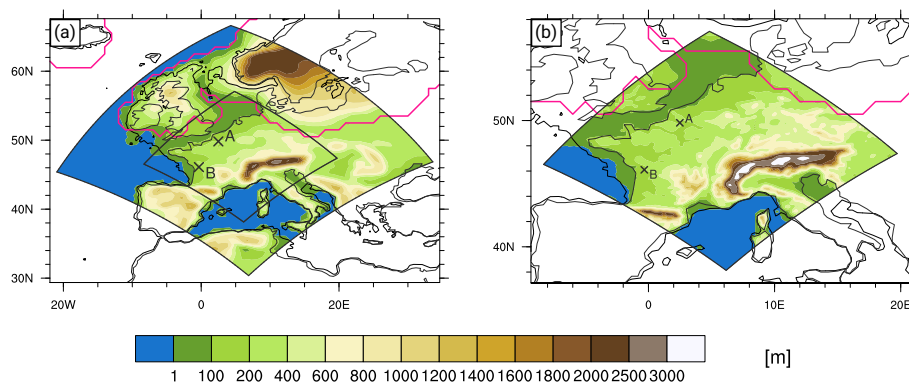
Figure 1. WRF model domain orography with LGM coastline (black line) and LGM ice sheet (pink line). *(a)* Domain 1 with 50 km grid spacing, *(b)* Domain 2 with 12.5 km grid spacing. Locations A and B on the map refer to time series of soil temperatures and soil temperature gradients in Fig. 7 and Fig. S5.
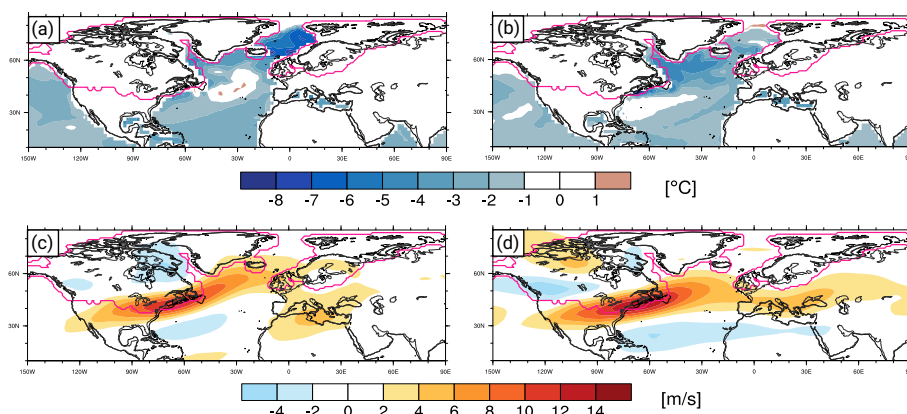
Figure 2. *(a)* Distribution of annual mean SST differences between the global MPI simulations under LGM and PI conditions. *(b)* as *(a)* but for the global AWI simulations. *(c)* and *(d)* as *(a)* and *(b)* but for the annual mean wind speed in 300 hPa.
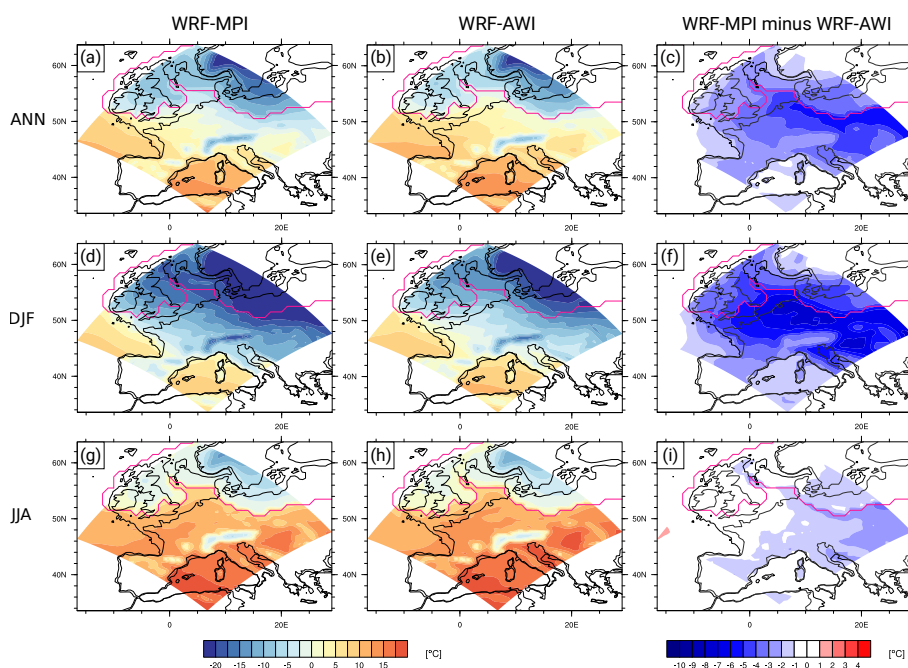
Figure 3. Distribution of 2 m air temperature in annual *(a-c)* and seasonal winter *(d-f)* and summer *(g-i)* means as simulated with the regional WRF model with MPI forcing *(a, d and g)* and with AWI forcing *(b, e and h)* and their differences *(c, f and i)*. Black line: LGM coastline, pink line: LGM ice sheet.
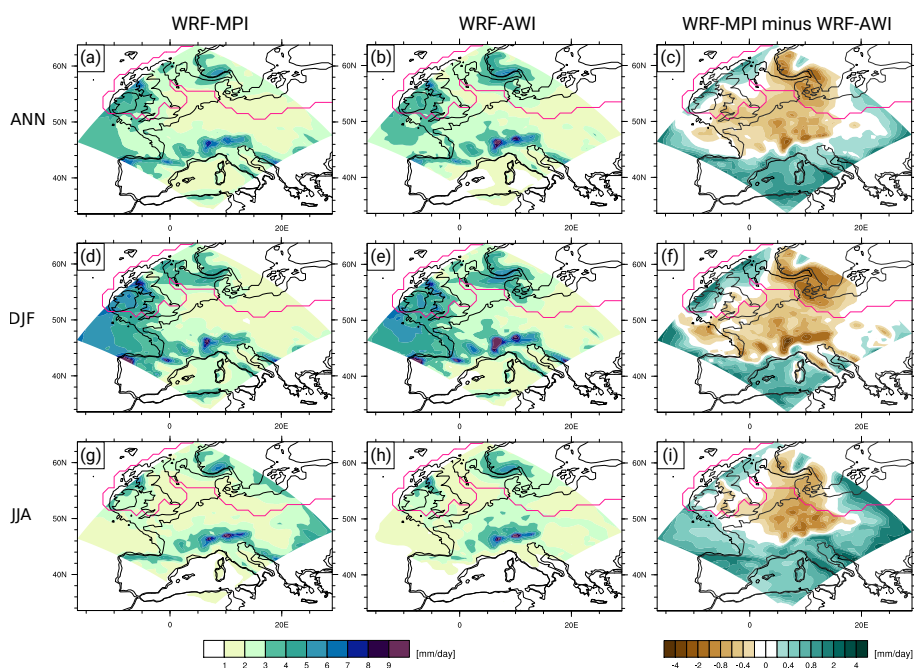
Figure 4. Distribution of total precipitation in annual *(a-c)* and seasonal winter *(d-f)* and summer *(g-i)* means as simulated with the regional WRF model with MPI forcing *(a, d and g)* and with AWI forcing *(b, e and h)* and their differences *(c, f and i)*. Black line: LGM coastline, pink line: LGM ice sheet.
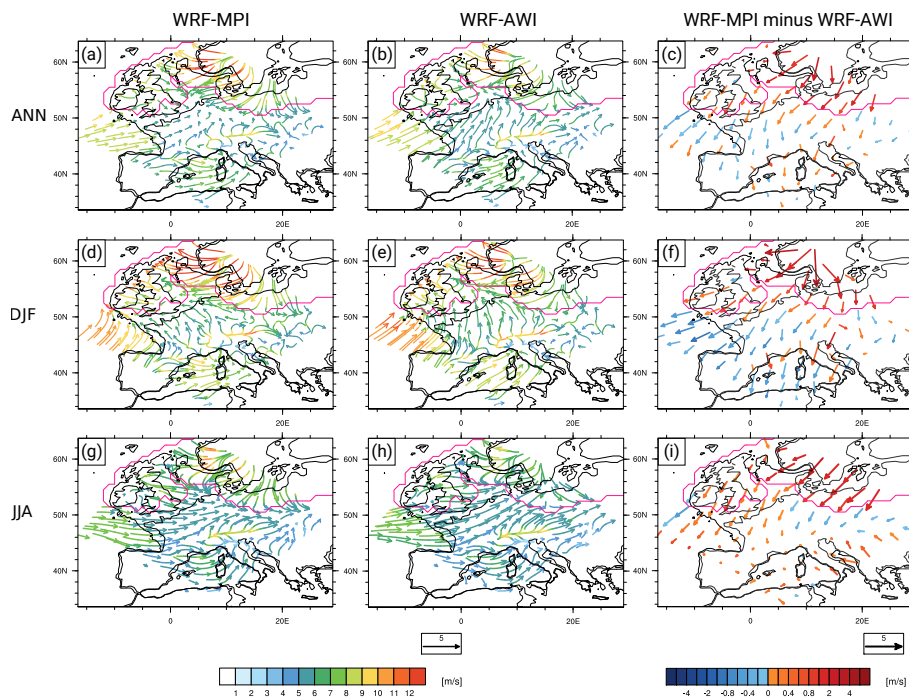
Figure 5. Distribution of 10 m wind speed in annual *(a-c)* and seasonal winter *(d-f)* and summer *(g-i)* means as simulated with the regional WRF model with MPI forcing *(a, d and g)* and with AWI forcing *(b, e and h)* and their differences *(c, f and i)*. Black line: LGM coastline, pink line: LGM ice sheet.
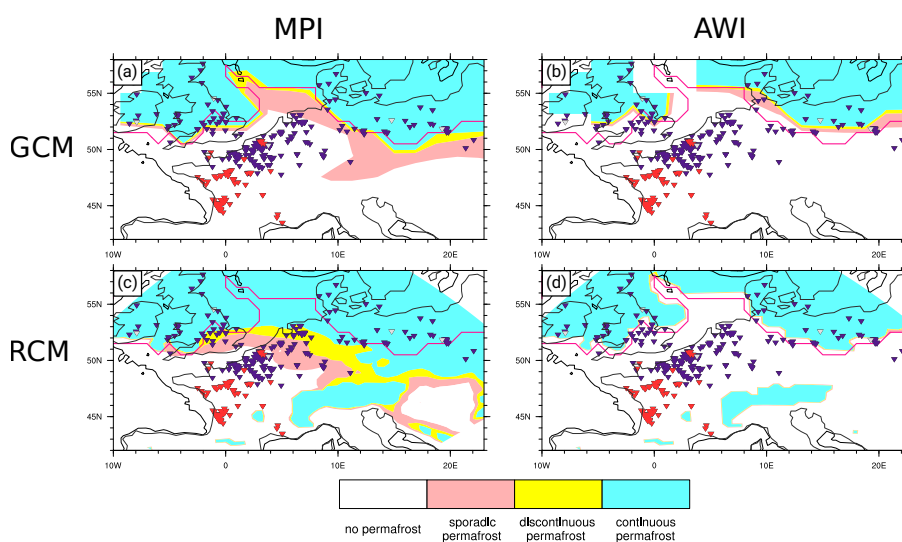
Figure 6. Permafrost distribution based on the surface frost index (SFI) in approximately 70 cm depth as simulated by the global MPI *(a)* and the global AWI simulation *(b)* and their respective regional counterpart *(c and d)*. Ice wedge pseudomorphs, composite, and sand wedges from Andrieux et al. (2016) and Isarin et al. (1998) are denoted by purple, grey, and red triangles respectively. Black line: LGM coastline, pink line: LGM ice sheet.
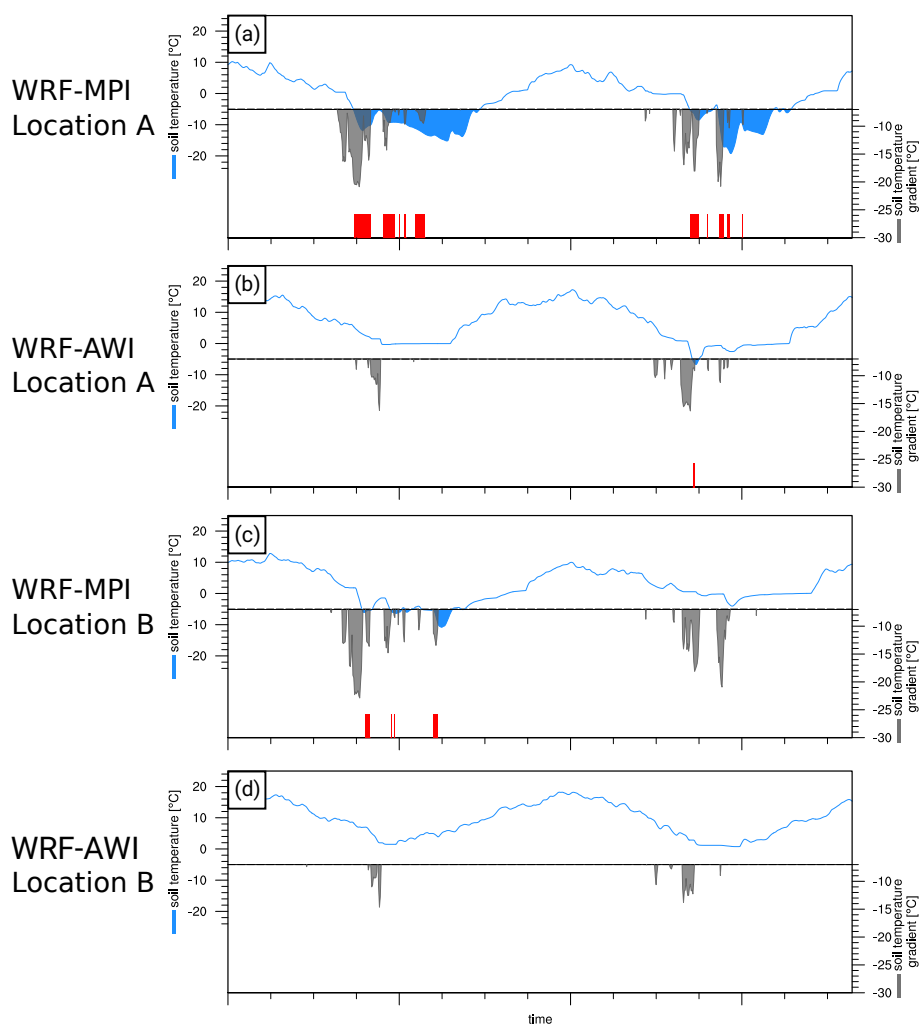
Figure 7. Time series of the daily mean soil temperature and soil temperature gradient in location A and B as denoted in Fig. 1 (A: model grid point 49.8° N, 2.49° E; B: model grid point 46.1° N, -0.33° E) as simulated in WRF-MPI *(a and c)* and in WRF-AWI *(b and d)* for two consecutive years. Blue lines show the development of the soil temperatures in layer 3 (70 cm). When the temperatures fall below -5 °C, the first condition for thermal contraction cracking after Matsuoka et al. (2018) is fulfilled, marked with blue shading and the reference line. The soil temperature gradient between the first layer (5 cm depth) and the third layer (grey shading) is only depicted when condition two after Matsuoka et al. (2018) is fulfilled, with a gradient below -7 °C. Red lines indicate the coincidence of the two conditions.
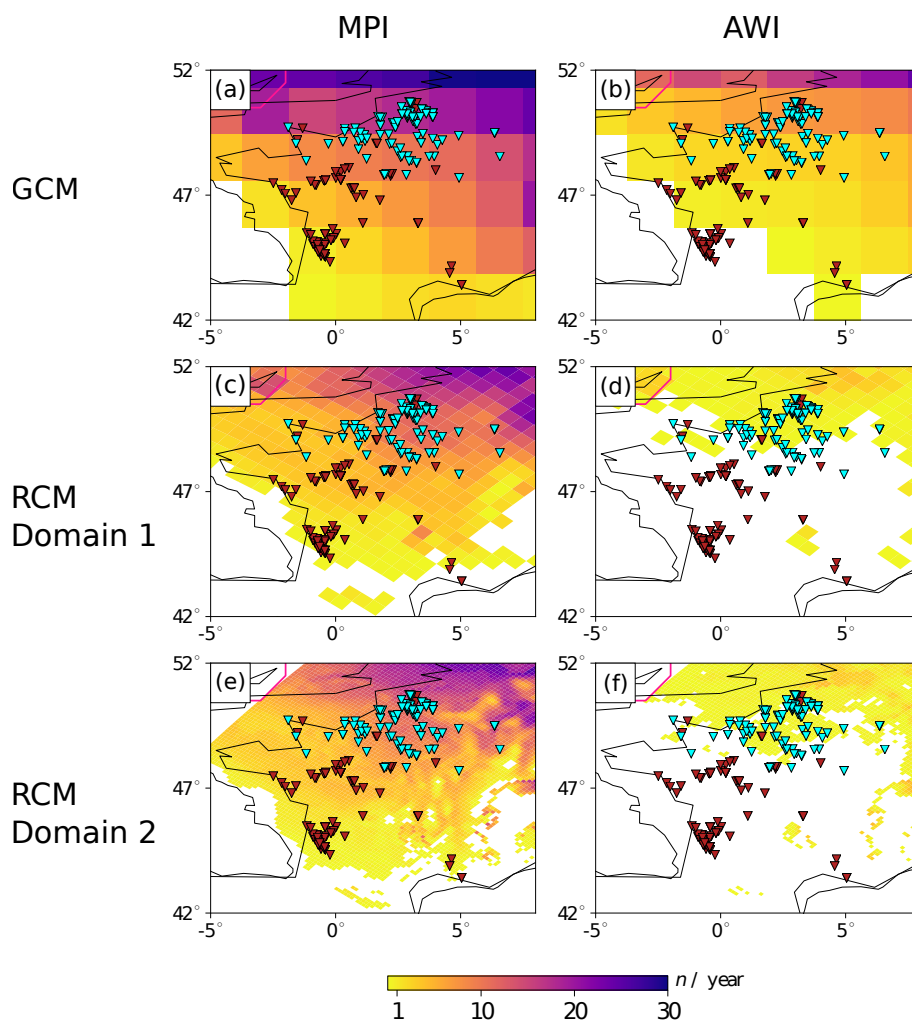
Figure 8. Heat maps of the mean number of days per year when the conditions for thermal contraction cracking after Matsuoka et al. (2018) are fulfilled for each grid box in the global MPI *(a)* and AWI simulations *(b)*, and for the first domain of the regional WRF-MPI *(c)* and WRF-AWI *(d)* simulations, as well as for the second domain in WRF-MPI *(e)* and in WRF-AWI *(f)*. Ice wedge pseudomorphs and sand wedges from Andrieux et al. (2016) are highlighted with cyan and red triangles, respectively, only when located in France. Black line: LGM coastline, gray line: LGM ice sheet.